photonics

MDPI

Article

The Phenomenon of Focal Shift Induced by Interface Reflection Loss in Microsphere-Assisted Imaging

Heying Zhang [1,2], Cong Zhai [2,*], Heming Jia [1], Yuzhen Guo [1,2], Bin Yao [2,3], Menghui Xiang [2,3], Danfeng Cui [1], Yongqiu Zheng [1], Yonghua Wang [1] and Chenyang Xue [1,2]

[1] State Key Laboratory of Extreme Environment Optoelectronic Dynamic Measurement Technology and Instrument, North University of China, Taiyuan 030051, China; s202306120@st.nuc.edu.cn (H.Z.); s202306052@st.nuc.edu.cn (H.J.); b20230616@st.nuc.edu.cn (Y.G.); cuidanfeng@nuc.edu.cn (D.C.); zhengyongqiu@nuc.edu.cn (Y.Z.); wangyonghua@nuc.edu.cn (Y.W.); xuechenyang@nuc.edu.cn (C.X.)
[2] Laoshan Laboratory, Qingdao 266237, China; yaobin24@stu.xmu.edu.cn (B.Y.); 19920230156573@stu.xmu.edu.cn (M.X.)
[3] Pen-Tung Sah Institute of Micro–Nano Science and Technology, Xiamen University, Xiamen 361102, China
* Correspondence: oliverchild@hotmail.com

Abstract

Microsphere-assisted super-resolution imaging technology, due to its ability to break through the diffraction limit, has become a powerful tool for achieving optical observations at the micro-nano scale. However, there remains a significant discrepancy between the simulation results of microsphere focusing behavior and experimental observations in existing studies, necessitating a more precise physical explanation. This study proposes that the interface reflection characteristics are a key factor influencing the focusing behavior of microspheres. We constructed a numerical simulation model based on ray optics theory using MATLAB, explicitly considering the reflection and transmission of light at the microsphere-medium boundary, and systematically analyzed the imaging process and focal position of the microsphere. Experimental results demonstrate that after accounting for energy loss due to reflection, the focal position obtained from the simulation calculations shows a high degree of consistency with the experimental results. The average deviation of our model from experimental results is reduced by 76% compared to conventional paraxial theory and by 86% compared to Finite-Difference Time-Domain (FDTD) simulations. Additionally, the findings validate the reliability of determining microsphere focusing theory using irradiance.

Keywords: microsphere; reflection; focus position; optical imaging

1. Introduction

Microsphere-assisted microscopic imaging is a technique that employs microspheres as optical elements to enhance the resolution and performance of microscopic imaging. This technology is compatible with existing microscopic systems and significantly increases the numerical aperture (NA) of the imaging system, thereby surpassing the diffraction limit [1–3]. It is an effective means to enhance the resolution of optical systems [4–6]. This technique offers a straightforward and economical approach to super-resolution imaging without the need for complex instruments or labeling techniques [7], allowing scientists to more easily observe intracellular structures, viral particles, and other subcellular details, thereby providing a groundbreaking observational tool across multiple fields [8,9].

Check for updates

Received: 4 February 2026
Revised: 13 February 2026
Accepted: 16 February 2026
Published: 19 February 2026

Copyright: © 2026 by the authors. Licensee MDPI, Basel, Switzerland. This article is an open access article distributed under the terms and conditions of the Creative Commons Attribution (CC BY) license.

Despite the significant achievements of microsphere-assisted microscopy techniques in experimental applications, various interpretations of its imaging mechanism still exist, and a unified theoretical framework has yet to be established [10]. At present, the Photonic Nanojet (PNJ) is regarded as a key mechanism [11,12]. It is a highly localized and intense optical field generated on the backlit side of dielectric microspheres, with a lateral dimension that can be smaller than the wavelength of the incident light, thereby providing micro-nano-level super-resolution imaging and manipulation [13–15]. However, it can only explain certain phenomena and characteristics and cannot be integrated with the actual imaging phenomenon of microspheres [16], which hinders the establishment of an effective model or relationship between imaging magnification and microspheres [17].

Alternative theories suggest that microspheres achieve super-resolution by capturing and amplifying evanescent waves, converting high-frequency sub-wavelength information into detectable far-field signals [18,19]. Nevertheless, this mechanism depends heavily on precise, nanoscale spacing between the sphere and sample, making it susceptible to environmental disturbances and leading to discrepancies in reproducibility [20]. Similarly, resonant whispering gallery modes (WGMs) can enhance local electromagnetic fields under specific conditions [21–23], but struggle to explain stable imaging behavior under broadband illumination or continuous parameter variations.

From a more intuitive perspective, transparent microspheres are often viewed as microlenses that focus light through refraction, similarly to traditional magnifying glasses [24,25]. This explanation provides a physical basis for understanding the magnification effect of microspheres. However, the focusing properties of small microspheres are highly sensitive to wavelength, which leads to image blurring and reduced resolution [26].

In summary, the imaging mechanism of microspheres remains largely unclear, and existing theories struggle to provide consistent and reliable explanations for experimental phenomena [25,27]. This also complicates the identification of the imaging plane that can achieve the highest resolution and best image contrast in practical applications.

Conventionally, in complex optical environments, the performance degradation caused by aberrations or scattering can be addressed by precisely modeling and correcting light-field disturbances to restore focus and resolution [28–31]. Inspired by this, we noticed that in microsphere imaging, the energy loss at the interface is often simplified or ignored. A rigorous ray-summation method developed by Brandsrud et al. for planar films demonstrates that accurate optical modeling requires accounting for all ray contributions with Fresnel equations at each interface [32]. Their work highlights the critical role of interface reflections, a principle that becomes even more pronounced in high-curvature microspheres. However, considering the extremely high curvature and refractive index mismatch of microspheres, this idealized energy loss is very likely to have a decisive impact on the actual imaging performance and focal field distribution.

Therefore, in order to provide a better physical explanation of the microsphere imaging mechanism and to more accurately locate its optimal imaging plane, this study aims to quantitatively assess the impact of interface reflection energy loss on the focusing characteristics of microspheres from a complementary research perspective. In our previous research, we introduced the concept of irradiance and relocated the imaging focus of microspheres through axial scanning methods [33]. Based on the understanding that irradiance is a key physical quantity determining the optical energy distribution at the imaging plane, we established a mathematical model for super-resolution imaging of microspheres using numerical simulation methods, further exploring the focusing effect of microspheres theoretically. The model calculates the energy loss of light each time it passes through the interface between the microsphere and the medium, and then determines the equivalent focal position by statistically analyzing the irradiance distribution along the

optical axis. Through systematic comparison with experimental results, we validated that this simulation model outperforms existing theories and simulation results in predicting focal positions. The findings of this study indicate that interface reflection energy loss is an important factor to consider when optimizing microsphere focusing models.

2. Modeling and Analysis

This study quantitatively investigates the impact of energy changes during optical phenomena such as refraction and reflection at the interface between microspheres and the surrounding medium on the final light field distribution. To achieve this, we constructed a ray-tracing theoretical model based on ray optics using MATLAB R2022a, comprehensively considering reflection characteristics when light enters the microsphere through another medium interface.

2.1. Ray-Tracing Model

To validate the effectiveness of the model, we selected a transparent sphere with typical parameters, specifically a diameter of 5 μm and a refractive index of 1.592, for simulation experiments aimed at observing and analyzing the position of its equivalent focal length. To accurately simulate the actual physical process, the refractive index of the external medium was set to 1.333, thereby mimicking the focusing effect of the microsphere in a water environment. The ray-tracing simulation uses 450 nm as the effective wavelength. Indeed, these parameter setting aligns with our previous experimental conditions [33]. Figure 1a shows the 3D simulation results of the model, which can visualize the deflection phenomenon of the light rays before and after entering the microspheres as well as the spatial distribution characteristics of the focusing effect. During the simulation, detailed behavioral data of each ray were recorded—including incidence point, refraction point, total reflection status, and final exit point—for subsequent processing and analysis to evaluate the sphere's effect on parallel beams, especially regarding focal point location and intensity distribution.

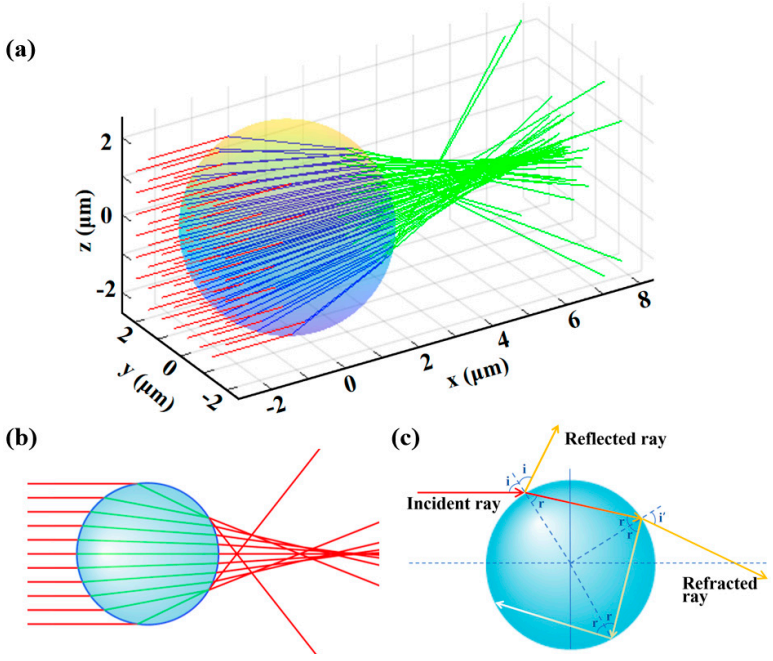


Figure 1. Simulation of light propagation process. (**a**,**b**) 3D view and 2D view of the microsphere simulation model. (**c**) A schematic diagram of the change in a single light ray in the propagation process, with lighter colors indicating less energy remaining in the light.

At the core of this simulation lies the ray-tracing algorithm, which handles interactions between rays and the lens. The incident rays are initialized with a deterministic uniform grid: all rays originate from the plane at $x = -1.5R$, uniformly distributed in a 100×100 grid along the y- and z-directions, covering the entire incident cross-section of the microsphere. The algorithm applies Snell's law to calculate angular changes when rays enter or exit the sphere. When the angle of incidence exceeds the critical angle, total internal reflection occurs at the spherical surface, preventing light from entering the interior [34]. The light that successfully enters the interior of the sphere undergoes refraction and reflection again when it reaches the other surface, until the light rays are completely detached from the sphere to locate the final exit angle and position.

When light passes through these spherical lenses, light rays close to the optical axis and edge rays away from the optical axis are refracted to different degrees due to the curvature of the lens, resulting in spherical aberration. Spherical aberration increases the size of the spot and shifts the best focus point to a position different from the calculated effective focal length, resulting in circular diffuse spots, the so-called "circle of confusion". Therefore, the microsphere does not have a single precise focal plane. Figure 1b shows the simulation effect of the two-dimensional section of the model, and the influence of spherical aberration can be intuitively seen.

2.2. Energy Attenuation and Transmission Characteristics

As light passes through a microsphere with a refractive index different from that of the surrounding medium, particle-internal caustics are formed inside the sphere due to refraction and multiple reflections, causing some light rays to be diminished in intensity as it exits the sphere. When light rays are incident from the center region of the microsphere, this region has the lowest density of light, but the intensity of an individual ray remains most intact, primarily due to the minimal loss of reflected energy it experiences during propagation. As the incident position moves towards the edge of the microsphere, the angle of the incident light that can be received becomes larger. Then, the energy loss caused by reflection during the propagation of the light is greater, resulting in a decreasing trend in the intensity of a single light ray, as illustrated in Figure 1c. Light encounters interfaces when entering and exiting microspheres, resulting in reflection losses at least twice.

Of particular note is the fact that extremely close to the edge of the microsphere, light rays are more likely to satisfy the total reflection condition and fail to transmit effectively, and although there are very few rays that theoretically satisfy the refraction condition that can penetrate the sphere, these rays also tend to experience the greatest degree of attenuation [35]. These effects are therefore particularly important for strongly inclined rays close to the edge of the sphere, which have large reflection coefficients [36].

The transmission characteristics of light through dielectric microspheres are governed by Fresnel's equations at each interface [37]. For an incident ray with an angle θ_i relative to the surface normal, the intensity reflection coefficients for s- and p-polarizations are given by Equations (1) and (2), respectively:

$$R_s = \left| \frac{n_1 \cos\theta_i - n_2 \sqrt{1 - \left(\frac{n_1}{n_2} \sin\theta_i\right)^2}}{n_1 \cos\theta_i + n_2 \sqrt{1 - \left(\frac{n_1}{n_2} \sin\theta_i\right)^2}} \right|^2 \quad (1)$$

$$R_p = \left| \frac{n_1 \sqrt{1 - \left(\frac{n_1}{n_2} \sin\theta_i\right)^2} - n_2 \cos\theta_i}{n_1 \sqrt{1 - \left(\frac{n_1}{n_2} \sin\theta_i\right)^2} + n_2 \cos\theta_i} \right|^2 \quad (2)$$

where n_1 and n_2 represent the refractive indices of the external medium and microsphere, respectively. The corresponding transmission coefficients are determined by energy conservation, as expressed in Equation (3):

$$T_s = 1 - R_s,\ T_p = 1 - R_p \tag{3}$$

For unpolarized illumination, the net transmittance at a single interface is given by averaging the s- and p-polarized components, as shown in Equation (4):

$$T_{\text{interface}} = \frac{T_s + T_p}{2} \tag{4}$$

When considering full traversal through the microsphere, the cumulative transmittance must account for multiple boundary interactions. For rays undergoing direct transmission without internal reflection ($k = 0$), the total transmittance is given by Equation (5):

$$T_{\text{total}}^{(0)} \approx T_1 \cdot T_2 \cdot T_{\text{material}} \tag{5}$$

where T_1 and T_2 denote transmittance at the entry and exit interfaces. $T_{\text{material}} = e^{-\beta l}$ represents the transmittance due to the attenuation of light within the microsphere material, accounting for losses from both absorption and bulk scattering. This exponential decay in intensity with propagation path length l is governed by the Beer-Lambert law. Here, β denotes the attenuation coefficient of the material, which characterizes the total loss per unit length.

For rays experiencing k internal reflections prior to emergence, the transmittance becomes more complex and is described by Equation (6):

$$T_{total}^{(k)}(\theta_i) = T_1(\theta_i) \cdot [R_{\text{int}}(\theta_i)]^k \cdot T_2(\theta_e) \cdot T_{material}^m \tag{6}$$

Here, R_{int} represents the internal reflection coefficient at the sphere-medium interface, calculated using Equations (1) and (2) with exchanged refractive indices ($n_1 \leftrightarrow n_2$). The integer $m = k + 1$ represents the number of internal chord segments traversed, corresponding to the total internal path length. The critical angle for total internal reflection is defined as: $\theta_c = \sin^{-1}\left(\frac{n_1}{n_2}\right)$.

Transmittance is an important parameter to measure the energy remaining after the light passes through the microsphere. Based on the above-mentioned transmittance formula derived from geometric optics theory and Fresnel's equation, we plotted the theoretical curves of the transmittance varying with the angle between the incident angle and the normal when the ray enters and leaves the microsphere [38], as shown in Figure 2. This curve indicates that the transmittance is highest under near-normal incidence conditions ($\theta_i \approx 0^\circ$). The number of reflections for edge rays increases dramatically, further reducing the light transmission. This distribution characteristic further suggests that the significant loss of edge rays leads to a decrease in the light intensity that should converge in front of the focal region, resulting in a backward shift in the position of the maximum light intensity.

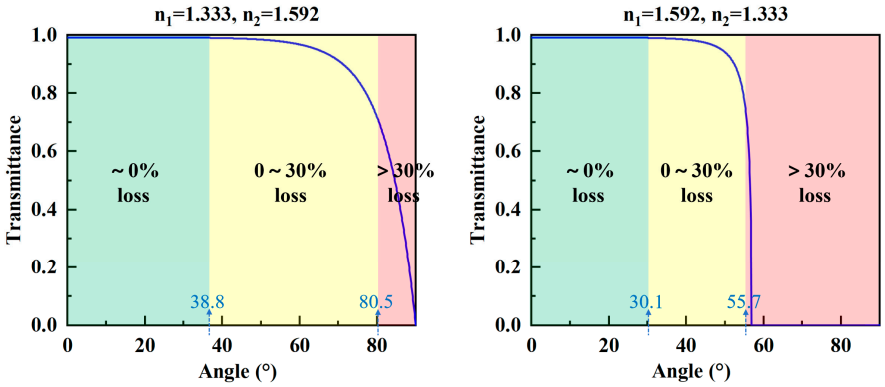


Figure 2. The transmittance of the light ray into and out of the microsphere varies with the angle between the light ray and the normal. When the angle between the light ray and the normal is in the green region, there is almost no energy loss; when the angle between the light ray and the normal is in the yellow region, the energy loss is less than 30%; when the angle between the light ray and the normal is in the red region, there is a large loss of energy. The blue numbers and dashed arrows indicate the threshold angles that define the boundaries between the green, yellow, and red regions.

2.3. Intensity Distribution and Effective Focal Point

When microspheres are placed on the sample, the incident light rays are focused by the microsphere to form a strongly localized spot in close proximity to the sample surface, thereby enabling super-resolution imaging. However, microspheres do not have a single precise focal plane. Therefore, finding the highest place of light convergence energy can realize better super-resolution imaging effect. We integrated the transmission effects on the light propagation path and on the change in energy, and set up numerous circular detectors of the same diameter with a spacing of 0.1 nm on the optical axis to simulate circles of confusion, as shown in Figure 3, consistent with the axial resolution of our experimental translation stage. This fine spacing is not strictly necessary and could be increased without loss of accuracy. Subsequently, the intensity of light gathered within each circular detector is quantified according to the intensity of the light ray that can pass through the circular detectors, which facilitates the analysis of physical optical propagation at different locations.

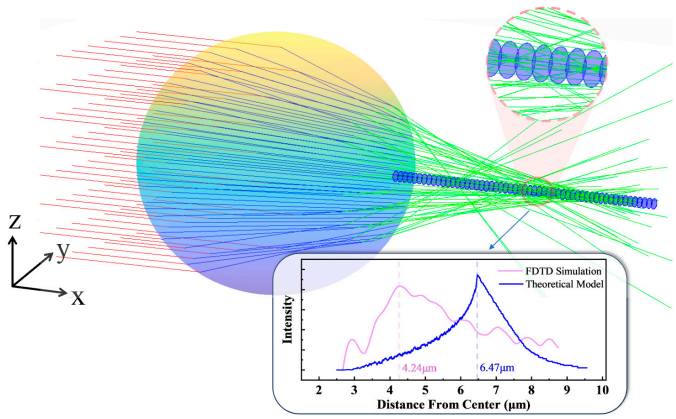


Figure 3. Schematic diagram of the microsphere focusing light intensity statistical method and its axial irradiance distribution data. The schematic illustrates the arrangement of a circular detector along the optical axis for monitoring light intensity at different positions. The blue curve in the data graph shows the normalized axial irradiance distribution, indicating that the light intensity reaches its maximum at approximately 6.47 μm from the center of the microsphere, which is identified as the effective focal point. The pink curve represents the distribution of light intensity of the microsphere along the optical axis under the PNJ effect. The light intensity reaches its maximum value at a distance of approximately 4.24 μm from the center of the microsphere.

Irradiance can directly reflect the spatial distribution of light energy. It essentially describes the condition of light energy distribution density during the transmission process [39]. After the refraction of light by the microspheres, the propagation path and energy distribution of light collectively determine the irradiance distribution in the space. Due to the rapid energy decay after each reflection, we set the maximum number of reflections to three. Tracking of a ray is terminated when its remaining energy falls below 0.1% of the initial value. The final intensity of each ray is given by $I = I_0 \cdot T_{\text{total}}$, where the expression for the total transmittance T_{total} is provided in Equation (6). By summing the energy of all light rays reaching the circular detector along the optical axis at each detector, a continuous axial irradiance distribution is generated. The precise positioning of the effective focus should correspond to the location where the light irradiance reaches its maximum. This is because the position of the focus is directly related to the spatial distribution density of the light energy.

The blue line in the data graph of Figure 3 illustrates the trend of light intensity variation within each circular detector as the distance from the lens increases, which also represents the distribution of axial irradiance. The effective focal point should be located at the position of maximum light intensity [40], which is approximately 6.47 μm from the center of the microsphere. In the same simulation environment, we employed the Finite-Difference Time-Domain (FDTD) algorithm in Ansys Lumerical FDTD 2024 R1 to simulate the changes in power density of the beam under the PNJ effect of the microsphere. The simulation results indicate that the position of the strongest focal point is at 4.24 μm, as shown by the pink line in the data graph of Figure 3. There is a certain discrepancy between the effective focal points obtained from both methods. However, compared to existing theories, the effective focal point derived from our model is closer to the actual observed imaging effects. The experiments will be detailed in the next chapter. This indicates that our proposed idea is more aligned with the true mechanism of microsphere imaging.

3. Experiment and Results

3.1. Longitudinal Imaging and Focus Positioning Experiment of 5 μm PS Microspheres

In our previous experiments [33], we performed longitudinal scanning imaging of a Blu-ray disc using polystyrene (PS) microspheres with a diameter of 5 μm under identical experimental conditions. Figure 4a illustrates a schematic diagram of the longitudinal scanning experiment assisted by microspheres. During the experiment, the movement platform carrying the Blu-ray disc was precisely controlled to step displace along the longitudinal (Z-axis) direction, thereby enabling scanning of the sample at different positions. During the imaging process, the microspheres formed an enlarged virtual image beneath them. As the disc sample moved relative to the microspheres and the imaging system in the Z direction, the images produced by the microspheres transitioned from a blurred state to a state of optimal clarity, and then back to a blurred state again. This reflects its higher-resolution imaging capability for sample structures within a specific spatial range. The actual imaging results are shown in Figure 4b.

The microscopic imaging system detects the imaging effect of the sample structure rather than the energy distribution of the spatial light field. Therefore, the experiment only obtains a series of two-dimensional image sequences through longitudinal scanning, which cannot directly measure the three-dimensional irradiance field. To accurately determine the position of the optimal imaging plane for the microspheres, we conducted a Fast Fourier Transform (FFT) analysis on images obtained from scanning different Z positions, based on the fundamental principles of optical imaging—namely, that image clarity is closely related to the intensity of spatial frequency components [41]. By calculating the power spectrum of each imaging plane, we extract the energy distribution characteristics in the frequency

domain. A higher peak power indicates that the image structural information of the plane is richer and the imaging is clearer, as shown in Figure 5c. Consequently, we obtain imaging quality assessment metrics corresponding to different Z positions. Combining this with the displacement data of the sample platform, we can further derive the effective focal length of the microsphere system at that position, thereby achieving precise localization of the optimal imaging plane.

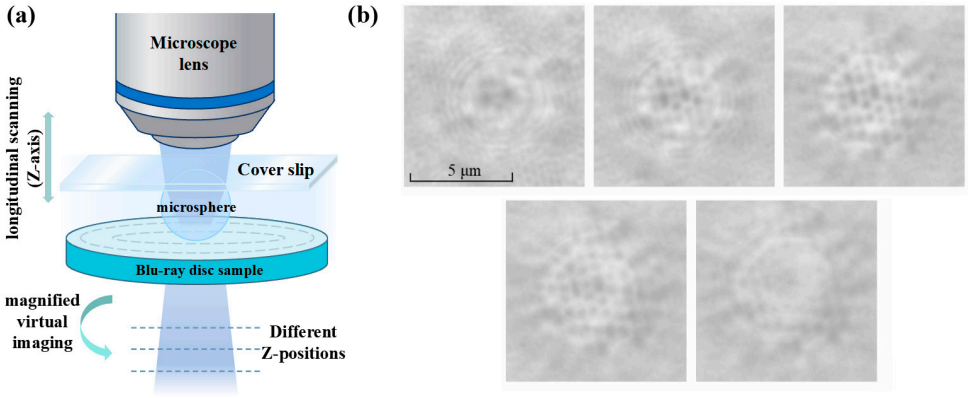


Figure 4. (**a**) Schematic diagram of the longitudinal scanning experiment of the microsphere imaging plane. (**b**) Imaging of Blu-ray discs assisted by microspheres. As the distance between the imaging plane and the microsphere increases, the observed imaging effect transitions from blurry to clear and then back to blurry.

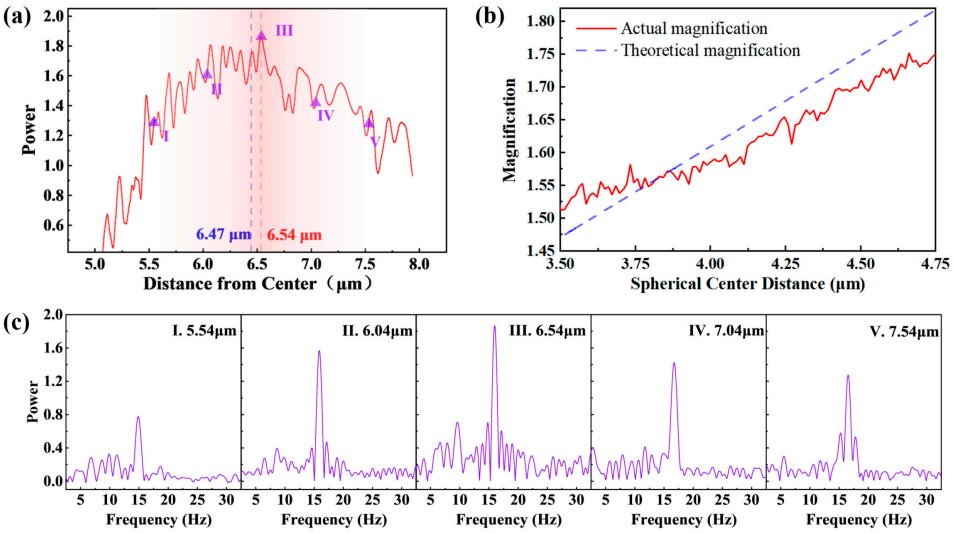


Figure 5. (**a**) The variation in the power spectrum of different imaging planes with respect to the focal length during the experiment. The Roman numerals (I–V) mark specific imaging planes selected for further analysis. The blue vertical line indicates the focal position derived from the theoretical model at 6.47 μm, while the red vertical line indicates the experimentally obtained focal position at 6.54 μm. (**b**) The red line indicates the magnification of microsphere imaging as the distance between the imaging plane and the sample plane changes in the experiment. Theoretically, the magnification of the microsphere should be a curve close to the blue dotted line. (**c**) The power spectrum data graphs obtained by performing FFT on the scanning images of five equally spaced imaging planes (corresponding to positions I–V). The higher the power, the clearer the image of the plane will be.

To minimize noise in the data while preserving the primary characteristics of the signal, we applied the Savitzky–Golay filtering method for smoothing the experimental data [42], resulting in the red curve shown in Figure 5a. As illustrated in the figure, the optimal imaging focal position for the microspheres identified in our experiment is 6.54 μm below

the center of the sphere. It is evident that the theoretical analysis value of 6.47 μm derived from our model is very close to the actual imaging result of 6.54 μm, and is significantly better than the simulation focus of 4.24 μm calculated using the FDTD method in the previous text.

Additionally, we further obtained the orbital periods of all scanned images. Using the scale of the microscope imaging without microspheres as a reference, we ultimately determined the magnification of the microspheres at different imaging planes, as indicated by the red line in Figure 5b. In addition, according to classical geometric optics theory, the magnification of a traditional single-focus convex lens increases linearly as the focal plane moves away [43], as shown by the blue line in Figure 5b. At the optimal imaging plane of the microspheres, the magnification was approximately 1.60×, which also has high consistency with the theoretical analysis results of 1.63×. Outside the optimal imaging plane, although there is some deviation between the two lines, there is still a high degree of trend consistency.

3.2. Comparative Experiments on Imaging Focal Points of Microspheres with Different Particle Sizes

To further validate the accuracy of the theoretical model established in Section 2 for predicting the focal position of microspheres and to assess the model's applicability under different particle size conditions, we conducted a series of experiments. In this experiment, DVD discs were selected as observation samples. Under the condition of water as the environmental medium, longitudinal scanning imaging experiments were performed on eight PS microspheres, with diameters distributed within the range of 10–11 μm. Under the same illumination conditions, a series of longitudinal images were collected by moving the focal plane along the optical axis. The spectral information of the image is obtained by using the FFT method, and then the power spectral information of each group of images is obtained, serving as a quantitative evaluation index for imaging clarity, and the optimal focal plane position for each microsphere was determined.

Based on this, we calculated the paraxial focal positions for each microsphere using traditional optics, as well as the focal positions obtained through electromagnetic simulations using the FDTD method. The paraxial theory relies on the ray propagation model and the paraxial approximation [44], which is commonly used for focal estimation in traditional optical systems, whereas FDTD is a full-wave electromagnetic simulation method based on Maxwell's equations, widely applied in the analysis of focusing characteristics of micro-nano optical structures.

Figure 6 summarizes the focal positions inferred from the best focal plane measured in the experiments, the predicted values from the simulation model, the results from the FDTD simulation, and the calculations based on paraxial theory. It can be observed that the deviation between the experimental data and the predicted values from the simulation model in this paper is significantly smaller than the deviations between the experimental data and the paraxial theory, as well as the deviations between the experimental data and the FDTD simulation results. Specifically, the maximum deviation between the paraxial theory and the experiment can reach up to 2.49 μm, while the maximum deviation between the FDTD simulation and the experiment is approximately 3.98 μm. In contrast, the maximum deviation between the predicted values from this model and the experimental results is only about 0.91 μm. Overall, the paraxial theory is based on the small-angle approximation, which neglects high-angle incident light and the spherical aberration it induces, leading to a significant underestimation of the actual focal position. Although the standard FDTD method can accurately solve Maxwell's equations and capture wave effects such as photon nanojet phenomena, it typically does not account for energy losses at the interface caused by reflection, resulting in predictions that place the focal point too

close to the surface of the microsphere. In contrast, the average deviation of the proposed model from experimental results is reduced by 76% compared to the paraxial theory and by 86% compared to the FDTD simulations. This result indicates that, compared with the two classical methods of traditional theory and wave optics, the optimization model of this paper exhibits higher experimental consistency in predicting the focal position of microspheres, and is able to more accurately reflect the focusing behavior of microspheres in actual imaging systems.

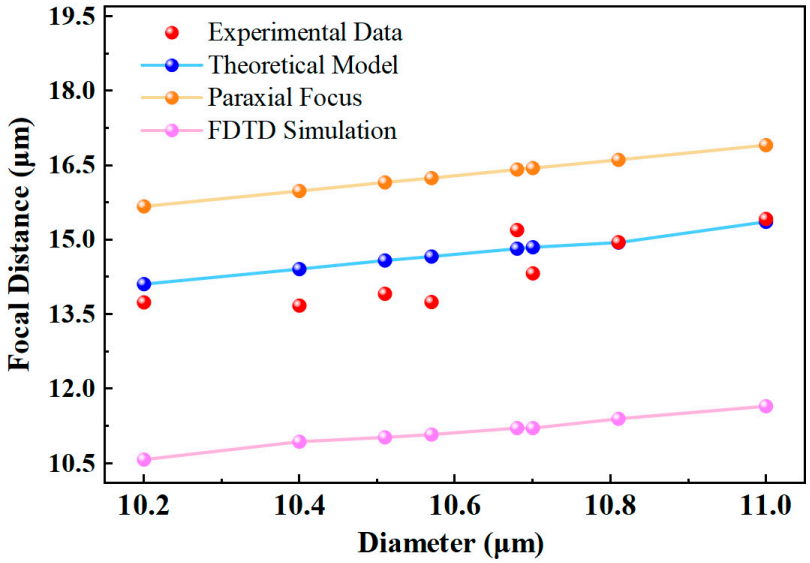


Figure 6. Comparison of focal positions of PS microspheres with diameters in the range of 10–11 μm in a water environment based on different theories. The red scatter points represent the focal positions of the microspheres derived from experimental data. The blue dashed line indicates the predicted results from the proposed theoretical model. The yellow line represents the results calculated using paraxial theory. The pink line shows the results obtained from FDTD simulation.

Although the experimental data closely aligns with the theoretical model predictions, certain discrepancies have been observed in the comparisons of some microspheres. It is important to note that the 10–11 μm microspheres used in this study are commercially sourced polydisperse samples, which have not been individually calibrated for size but are provided as a nominal size range. To obtain the specific size of each microsphere, we measured them individually using an optical microscope during the experiment. However, due to issues such as thick imaging edges and blurriness, the measurement results exhibit a degree of subjectivity and uncertainty, leading to size errors.

Additionally, the experiments observed that the equivalent optical center of the microsphere lens may not be located at the geometric centroid of the microsphere. Most of the data points obtained from the experiments exhibited a unidirectional deviation trend, indicating the presence of a systematic shift. Such phenomena are more pronounced in high refractive index microsphere systems.

In summary, these experiments not only verified the applicability and accuracy of the optimization model of this paper for microspheres of different particle sizes, but also provided a key reference for understanding the actual imaging mechanism of microspheres. The modeling approach and the equivalent focus method established in this paper lay a foundation for further research to explore the real physical mechanism of microsphere imaging in depth.

4. Discussion

The results of this study provide a more intuitive explanation for the long-standing discrepancy between theoretical predictions and experimental observations in the field of microsphere-assisted super-resolution imaging. By explicitly incorporating the energy loss due to Fresnel reflection at the microsphere-medium interface into a geometrical optics-based model, we have achieved a closer alignment between the simulation results and the experimental observations. The predictive accuracy of the simulations significantly surpasses that of traditional paraxial theories and the FDTD full-wave simulation methods.

This work addresses a critical gap in the existing literature. Although the photon nanojet effect has been widely accepted as one of the primary mechanisms for achieving super-resolution, the predicted focal plane position has consistently been systematically smaller than the optimal imaging plane position observed experimentally [13,14]. This systematic deviation suggests that while the FDTD full-wave electromagnetic model is powerful in capturing near-field fluctuation phenomena, it may overlook a key factor: the cumulative energy attenuation of light during propagation, particularly for light at large incident angles. Our results indicate that high-angle 'edge rays' suffer significant reflective losses at the interface, causing the effective focal point to shift from the PNJ hotspot towards the far field. The accuracy of the effective focal point prediction has improved after considering the energy loss due to reflection.

Establishing irradiance as a key physical quantity for determining the optimal imaging plane for microsphere imaging is another significant contribution of this study. Yang et al. explicitly pointed out in their representative research that the super-resolution capability of microspheres is determined by the waist of the PNJ, with the minimum waist corresponding to the best resolution [12]. However, this work did not address the crucial practical question of "the location of the optimal imaging plane". Our research precisely fills this gap: by introducing an interface energy loss model and using axial irradiance as a criterion, we provide a practical method for quantitatively predicting the optimal imaging position.

In our previous research, it was noted that irradiance is a key factor determining the imaging quality of microspheres, and that microspheres do not possess a singular geometric focus [33]. However, the underlying physical mechanism remains unclear; it merely elevates the issue of focus from the geometric optics level to the energy distribution level. This study further reveals that the non-uniform energy loss caused by interface reflection is the fundamental reason for the systematic shift in the effective focus of microspheres. As demonstrated in the rigorous ray-summation framework for planar films [32], properly accounting for such interface effects is essential for accurate optical modeling. In traditional microscopy, the focus is typically associated with the position of the minimum light spot. However, in complex systems like microspheres, which exhibit severe aberrations and cannot form a single sharp focus, the concept of the "circle of confusion" is more applicable. We calculate the distribution of axial irradiance by integrating the total optical energy at various points along the optical axis behind the microsphere, providing a robust and physically meaningful metric. This metric is directly related to image quality, which has been validated through FFT-based clarity analysis.

Furthermore, for the FDTD simulation, the maximum intensity of PNJ does not necessarily correspond to the optimal imaging plane. As pointed out by Maslov et al., there is an essential distinction between the point spread function (PSF) that determines image resolution and the field distribution of PNJ [15]. FDTD can accurately capture complex interference patterns and near-field resonances, producing high-intensity 'hot spots'. However, these hot spots do not always coincide with the planes that yield the best clarity or magnification in actual microscopic systems. In contrast, our model focuses on the statistical distribution of irradiance and the effective convergence of light, which is

physically closer to the concept of the 'effective focal point' that is coupled through the objective lens and ultimately recorded by the camera.

The FDTD simulation itself faces issues related to computational cost. In microsphere-assisted imaging experiments, the illuminating light is typically incoherent. As pointed out by Pahl et al. [45], in this case, light from different incident angles cannot superimpose the electric fields, but rather their respective intensities should be summed. Therefore, to accurately predict imaging results through full-wave simulations, a separate simulation must be conducted for each incident angle, followed by summing the resulting intensities. For three-dimensional microspheres, this computational demand is substantial and often difficult to achieve. Our model is based on the ray-tracing method, which is more direct in handling light rays. By applying energy weighting to the rays, the final irradiance distribution is obtained by accumulating the energy contributions of all rays. Therefore, it provides a predictive tool that combines universality and computational efficiency, applicable to various microsphere sizes and lighting conditions.

Of course, this model also has its applicable scope. The minimum diameter of the microspheres studied in this paper is 5 μm, corresponding to $D/\lambda \approx 11 (\lambda \approx 450\ \text{nm})$. At this scale, diffraction, astigmatism, and other wave effects are relatively weak compared to geometric refraction and reflection, allowing the ray-tracing method to approximately describe the primary focusing behavior. However, for the precise characterization of near-field fine structures and sub-wavelength scale field enhancements, full-wave electromagnetic simulation remains an irreplaceable tool.

When the structural dimensions approach the order of the wavelength, the material interfaces may no longer exhibit clear geometric boundaries, but instead present a blurred region influenced by critical behaviors of total internal reflection and other boundary conditions. This uncertainty in boundary behavior at the microscopic scale significantly affects the focusing efficiency and position of energy within the microsphere. In the future, combining the efficient path analysis advantages of geometric optics with the accurate solving capabilities of wave optics for electromagnetic field distributions, such as considering the non-ideal transmission characteristics of material interfaces in simulations, may contribute to a more accurate revelation of the true focusing physical processes in micro-scale lens systems. Moving forward, we will conduct collaborative research on multi-scale modeling to further deepen our understanding of the focusing behavior of microspheres.

5. Conclusions

This study constructs a numerical simulation model based on ray optics, focusing on the energy loss effects caused by interface reflections during the imaging process of microspheres. Both theoretical modeling and experimental validation indicate that this effect is a key physical factor leading to the deviation of microsphere focusing characteristics from actual imaging in other simulation results. This is particularly evident in the higher reflection loss of edge rays due to their large-angle incidence, as well as its significant impact on the light field irradiance distribution and the final equivalent focal position. The results confirm that the optimized model developed in this study significantly improves prediction accuracy, with a maximum focal position error of only approximately 0.91 μm, which is far superior to conventional approaches. The work also validates maximum irradiance as a reliable criterion for determining the equivalent focal point, underscoring that microsphere imaging adheres to energy conservation and light propagation principles. In previous studies of wave optics simulations, systematic deviations may have been introduced due to the neglect of actual energy changes at the interface. This study provides a quantifiable and verifiable modeling approach for this field, as well as a method for determining the

equivalent focal point of microspheres and the optimal imaging plane. In the future, we will incorporate energy boundary conditions that align more closely with physical realities into wave optical simulation in order to jointly advance the comprehensive understanding and optimization of microsphere imaging mechanisms.

Author Contributions: Conceptualization, H.Z. and C.Z.; methodology, H.Z. and C.Z.; software, H.Z., H.J. and B.Y.; validation, H.J., M.X. and D.C.; formal analysis, H.Z.; investigation, H.Z.; resources, Y.G. and C.X.; data curation, Y.G. and C.Z.; writing—original draft preparation, H.Z.; writing—review and editing, C.Z. and Y.Z.; visualization, H.J. and B.Y.; supervision, D.C., Y.W. and C.X.; project administration, C.Z. and Y.Z.; funding acquisition, C.Z. and C.X. All authors have read and agreed to the published version of the manuscript.

Funding: The National Natural Science Foundation of China (62405294), the Fundamental Research Program of Shanxi Province (202403021222157), and the Postgraduate research innovation Project of Shanxi Province (2024KY583).

Institutional Review Board Statement: Not applicable.

Informed Consent Statement: Not applicable.

Data Availability Statement: All data generated in this study are shown in this manuscript.

Conflicts of Interest: The authors declare no conflicts of interest.

Abbreviations

The following abbreviations are used in this manuscript:

PNJ	Photonic Nanojet
NA	numerical aperture
WGMs	Whispering Gallery Modes
PS	Polystyrene
FFT	Fast Fourier Transform
FDTD	Finite-Difference Time-Domain
PSF	point spread function

References

1. Wang, Z.; Guo, W.; Li, L.; Luk'yanchuk, B.; Khan, A.; Liu, Z.; Chen, Z.; Hong, M. Optical Virtual Imaging at 50 Nm Lateral Resolution with a White-Light Nanoscope. *Nat. Commun.* **2011**, *2*, 218. [CrossRef] [PubMed]
2. Moon, J.S.; Lee, H.; Lee, J.H.; Jeon, W.B.; Lee, D.; Lee, J.; Paik, S.; Han, S.-W.; Reuter, R.; Denisenko, A.; et al. High-Resolution, High-Contrast Optical In-terface for Defect Qubits. *ACS Photonics* **2021**, *8*, 2642–2649. [CrossRef]
3. Zhu, H.; Fan, W.; Zhou, S.; Chen, M.; Wu, L. Polymer Colloidal Sphere-Based Hybrid Solid Immersion Lens for Optical Super-Resolution Imaging. *ACS Nano* **2016**, *10*, 9755–9761. [CrossRef] [PubMed]
4. Liu, X.; Hu, S.; Tang, Y. Coated High-Refractive-Index Barium Titanate Glass Microspheres for Optically Trapped Microsphere Super-Resolution Microscopy: A Simulation Study. *Photonics* **2020**, *7*, 84. [CrossRef]
5. Jiang, W.; Wang, J.; Yang, Y.; Bu, Y. A Review of Microsphere Super-Resolution Imaging Techniques. *Sensors* **2024**, *24*, 2511. [CrossRef]
6. Darafsheh, A.; Limberopoulos, N.I.; Derov, J.S.; Walker, D.E.; Astratov, V.N. Advantages of Microsphere-Assisted Super-Resolution Imaging Technique over Solid Immersion Lens and Confocal Microscopies. *Appl. Phys. Lett.* **2014**, *104*, 061117. [CrossRef]
7. Zhu, H.; Yan, B.; Zhou, S.; Wang, Z.; Wu, L. Synthesis and Super-Resolution Imaging Performance of a Refractive-Index-Controllable Microsphere Superlens. *J. Mater. Chem. C* **2015**, *3*, 10907–10915. [CrossRef]
8. Ben-Aryeh, Y. Nano-Jet Related to Bessel Beams and to Su-per-Resolutions in Microsphere Optical Experiments. *EPJ Tech. Instrum.* **2017**, *4*, 3. [CrossRef]
9. Li, L.; Guo, W.; Yan, Y.; Lee, S.; Wang, T. Label-Free Super-Resolution Imaging of Adenoviruses by Submerged Microsphere Optical Nanoscopy. *Light Sci. Appl.* **2013**, *2*, e104. [CrossRef]
10. Yan, Y.; Li, L.; Feng, C.; Guo, W.; Lee, S.; Hong, M. Microsphere-Coupled Scanning Laser Confocal Nanoscope for Sub-Diffraction-Limited Imaging at 25 Nm Lateral Resolution in the Visible Spectrum. *ACS Nano* **2014**, *8*, 1809–1816. [CrossRef]

11. Yang, H.; Gijs, M.A.M. Optical Microscopy Using a Glass Microsphere for Metrology of Sub-Wavelength Nanostructures. *Microelectron. Eng.* **2015**, *143*, 86–90. [CrossRef]
12. Yang, H.; Trouillon, R.; Huszka, G.; Gijs, M.A.M. Super-Resolution Imaging of a Dielectric Microsphere Is Governed by the Waist of Its Photonic Nanojet. *Nano Lett.* **2016**, *16*, 4862–4870. [CrossRef] [PubMed]
13. Darafsheh, A. Photonic Nanojets and Their Applications. *J. Phys. Photonics* **2021**, *3*, 022001. [CrossRef]
14. Luk'yanchuk, B.S.; Paniagua-Domínguez, R.; Minin, I.; Minin, O.; Wang, Z. Refractive Index Less than Two: Photonic Nanojets Yesterday, Today and Tomorrow [Invited]. *Opt. Mater. Express* **2017**, *7*, 1820–1847. [CrossRef]
15. Maslov, A.V.; Astratov, V.N. Resolution and Reciprocity in Microspherical Nanoscopy: Point-Spread Function Versus Photonic Nanojets. *Phys. Rev. Appl.* **2019**, *11*, 064004. [CrossRef]
16. Maslov, A.V.; Astratov, V.N. Origin of the Super-Resolution of Microsphere-Assisted Imaging. *Appl. Phys. Lett.* **2024**, *124*, 061105. [CrossRef]
17. Duan, Y.; Barbastathis, G.; Zhang, B. Classical Imaging Theory of a Microlens with Super-Resolution. *Opt. Lett.* **2013**, *38*, 2988–2990. [CrossRef]
18. Yang, S.; Ye, Y.-H.; Shi, Q.; Zhang, J. Converting Evanescent Waves into Propagating Waves: The Super-Resolution Mechanism in Microsphere-Assisted Microscopy. *J. Phys. Chem. C* **2020**, *124*, 25951–25956. [CrossRef]
19. Boudoukha, R.; Perrin, S.; Demagh, A.; Montgomery, P.; Demagh, N.-E.; Lecler, S. Near- to Far-Field Coupling of Evanescent Waves by Glass Microspheres. *Photonics* **2021**, *8*, 73. [CrossRef]
20. Yao, L.; Lu, Y.; Yue, L.; Wang, Y.; Cong, Z.; Sun, Y.; Dong, T.; Jiang, C.; Wang, Z. Detection of Picometer Scale Vibration Based on the Microsphere Near-Field Probe. *Measurement* **2025**, *242*, 115892. [CrossRef]
21. Abbasian, V.; Pahl, T.; Hüser, L.; Lecler, S.; Montgomery, P.; Lehmann, P.; Darafsheh, A. Microsphere-Assisted Quantitative Phase Microscopy: A Review. *Light Adv. Manuf.* **2024**, *5*, 133–152. [CrossRef]
22. Zhou, S.; Deng, Y.; Zhou, W.; Yu, M.; Urbach, H.P.; Wu, Y. Effects of Whispering Gallery Mode in Microsphere Super-Resolution Imaging. *Appl. Phys. B* **2017**, *123*, 236. [CrossRef]
23. Hoang, T.X.; Duan, Y.; Chen, X.; Barbastathis, G. Focusing and Imaging in Microsphere-Based Microscopy. *Opt. Express* **2015**, *23*, 12337–12353. [CrossRef]
24. Lin, Q.; Liu, H.; Kang, Y. Investigation of Far-Field Super-Resolution Imaging by Microsphere-Based Optical Microscopy. *Opt. Lasers Eng.* **2021**, *144*, 106644. [CrossRef]
25. Darafsheh, A. Microsphere-Assisted Microscopy. *J. Appl. Phys.* **2022**, *131*, 031102. [CrossRef]
26. Liu, Y.; Liu, H.; He, L.; Zhou, H.; Sui, C. Broadband Dispersion Characteristics of Diffractive Microlenses Based on the Finite-Difference Time-Domain Method. *Opt. Laser Technol.* **2010**, *42*, 1286–1293. [CrossRef]
27. Chen, L.; Zhou, Y.; Li, Y.; Hong, M. Microsphere Enhanced Optical Imaging and Patterning: From Physics to Applications. *Appl. Phys. Rev.* **2019**, *6*, 021304. [CrossRef]
28. Brandsrud, M.A.; Blümel, R.; Solheim, J.H.; Kohler, A. The Effect of Deformation of Absorbing Scatterers on Mie-Type Signatures in Infrared Microspectroscopy. *Sci. Rep.* **2021**, *11*, 4675. [CrossRef]
29. Hillman, T.R.; Yamauchi, T.; Choi, W.; Dasari, R.R.; Feld, M.S.; Park, Y.; Yaqoob, Z. Digital Optical Phase Conjugation for Delivering Two-Dimensional Images through Turbid Media. *Sci. Rep.* **2013**, *3*, 1909. [CrossRef]
30. Matthews, T.E.; Medina, M.; Maher, J.R.; Levinson, H.; Brown, W.J.; Wax, A. Deep Tissue Imaging Using Spectroscopic Analysis of Multiply Scattered Light. *Optica* **2014**, *1*, 105–111. [CrossRef]
31. Samarkin, V.; Alexandrov, A.; Galaktionov, I.; Kudryashov, A.; Nikitin, A.; Rukosuev, A.; Toporovsky, V.; Sheldakova, J. Wide-Aperture Bimorph Deformable Mirror for Beam Focusing in 4.2 PW Ti:Sa Laser. *Appl. Sci.* **2022**, *12*, 1144. [CrossRef]
32. Brandsrud, M.A.; Blümel, R.; You, C.C.; Marstein, E.S.; Seim, E.; Lukacs, R.; Olsen, E.; Kohler, A. An Exact Ray Model for Oblique Incident Light on Planar Films. *Phys. E Low-Dimens. Syst. Nanostruct.* **2021**, *126*, 114374. [CrossRef]
33. Zhai, C.; Hong, Y.; Lin, Z.; Chen, Y.; Guo, M.; Guo, T.; Wang, H.; Hu, C. Addressing the Imaging Limitations of a Microsphere-Assisted Nanoscope. *Opt. Express* **2022**, *30*, 39417–39430. [CrossRef] [PubMed]
34. Hao, X.; Kuang, C.; Liu, X.; Zhang, H.; Li, Y. Microsphere Based Microscope with Optical Super-Resolution Capability. *Appl. Phys. Lett.* **2011**, *99*, 203102. [CrossRef]
35. Jha, A.K.; Zhu, Y.; Arridge, S.; Wong, D.F.; Rahmim, A. Incorporating Reflection Boundary Conditions in the Neumann Series Radiative Transport Equation: Application to Photon Propagation and Reconstruction in Diffuse Optical Imaging. *Biomed. Opt. Express* **2018**, *9*, 1389. [CrossRef]
36. Luk'yanchuk, B.S.; Arnold, N.; Huang, S.M.; Wang, Z.B.; Hong, M.H. Three-Dimensional Effects in Dry Laser Cleaning. *Appl. Phys. A* **2003**, *77*, 209–215. [CrossRef]
37. Ma, X.; Zheng, H.; Tian, M. Optimize the Shape of Curved-Fresnel Lens to Maximize Its Transmittance. *Sol. Energy* **2016**, *127*, 285–293. [CrossRef]
38. Rangel-Cárdenas, J.; Sobral, H. Optical Absorption Enhance-ment in CdTe Thin Films by Microstructuration of the Silicon Substrate. *Materials* **2017**, *10*, 607. [CrossRef]

39. Reshidko, D.; Sasian, J. Role of Aberrations in the Relative Illumination of a Lens System. *Opt. Eng.* **2016**, *55*, 115105. [CrossRef]
40. Nasibov, H. Evaluation of Focus Measures for Hyperspectral Imaging Microscopy Using Principal Component Analysis. *J. Imaging* **2024**, *10*, 240. [CrossRef]
41. Liu, Y.; Fang, F.; Wang, T.; Li, J.; Sheng, Y.; Zhang, G. Multi-Scale Grid Network for Image Deblurring with High-Frequency Guidance. *IEEE Trans. Multimed.* **2022**, *24*, 2890–2901. [CrossRef]
42. Wu, R.; Li, Y.; Zhang, S. Strain Fields Measurement Using Frequency Domain Savitzky–Golay Filters in Digital Image Correlation. *Meas. Sci. Technol.* **2023**, *34*, 095115. [CrossRef]
43. Chen, L.-W.; Zhou, Y.; Wu, M.-X.; Hong, M.-H. Remote-Mode Microsphere Nano-Imaging: New Boundaries for Optical Microscopes. *Opto-Electron. Adv.* **2018**, *1*, 17000101. [CrossRef]
44. Carpena, P.; Coronado, A.V. On the Focal Point of a Lens: Beyond the Paraxial Approximation. *Eur. J. Phys.* **2006**, *27*, 231–241. [CrossRef]
45. Pahl, T.; Hüser, L.; Hagemeier, S.; Lehmann, P. FEM-Based Modeling of Microsphere-Enhanced Interferometry. *Light Adv. Manuf.* **2022**, *3*, 699–711. [CrossRef]

Disclaimer/Publisher's Note: The statements, opinions and data contained in all publications are solely those of the individual author(s) and contributor(s) and not of MDPI and/or the editor(s). MDPI and/or the editor(s) disclaim responsibility for any injury to people or property resulting from any ideas, methods, instructions or products referred to in the content.